Robotics and Autonomous Systems 175 (2024) 104662

Contents lists available at ScienceDirect

Robotics and Autonomous Systems

journal homepage: www.elsevier.com/locate/robot

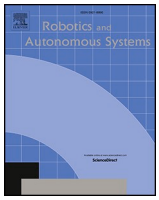

Design and stabilization of a Coandă effect-based UAV: Comparative study between fuzzy logic and PID control approaches

Tomás de J. Mateo Sanguino *, José M. Lozano Domínguez

University of Huelva, Dep. Ingeniería Electrónica, Sistemas Informáticos y Automática, Ctra. Huelva-La Rábida S/N, 21819 Palos de la Frontera, Huelva, Spain

ARTICLE INFO

Keywords:
Coanda effect
Fuzzy model
Intelligent control system
Mechatronic design
UAV

ABSTRACT

Recent years have experienced a notable surge in unmanned aerial vehicles (UAV) research, prompting exploration into innovative concepts. This paper introduces a compact UAV harnessing the Coandă effect, an underexplored phenomenon in fluid mechanics. Featuring a single lift motor and two types of flaps, this UAV offers exceptional maneuverability, presenting significant challenges compared to conventional multi-rotor UAVs. To address these challenges, we explore the theoretical study, mechatronic design, and manufacturing complexities of the Coandă UAV. Emphasizing the distinctiveness of our work, we assess a Fuzzy Logic Controller (FLC) for UAV stabilization, marking the first application of such techniques to a Coandă-effect UAV, in contrast to the Proportional-Integral-Derivative (PID) control employed by other researchers. This innovative application of Fuzzy logic, particularly the Sugeno model, proves advantageous, offering faster and more robust control in uncertain or noisy environments. The proposed FLC strategy is systematically compared against a classical PID control approach, formulated based on the Mamdani and Sugeno models, optimized and manually tuned using a genetic algorithm. Our results showcase a significantly improved settling time of 0.417 s with the FLC strategy, surpassing the PID control approach by 35.23%. To substantiate our findings, we present comprehensive experimentation conducted at both software and hardware levels using Matlab® and Simulink for a microcontroller-based UAV. This groundbreaking fusion of novel design and advanced control techniques not only addresses the unique challenges posed by the Coandă UAV's aerodynamics but also contributes significantly to the field of UAV research.

1. Introduction

The research and development of UAVs have exponentially grown nowadays unlike more traditional research fields —as mobile robotics, humanoid robotics, underwater robotics or the intelligent autonomous ground vehicles (AGVs)— due to the faster and more profitable scientific return at a lower cost [1]. Despite of the variety of sizes, designs and purposes, most of the UAVs are predominantly based on classical planes with a fixed-wing design (55.74%) and to a lesser extent on rotary vertical take-off and landing (VTOL) aircrafts (26.43%), and hybrid UAVs (17.82%) as studied through [2–5], among others.

The main advantages of the Coandă phenomenon applied to UAVs are: (*i*) higher energetic efficiency, (*ii*) good ratio of payload vs total weight, and (*iii*) high maneuverability. This approach addresses the lower maneuverability of fixed-wing aircrafts with better energy use compared to conventional UAVs [6]. The application of intelligent control systems helps to successfully pilot UAVs. It becomes more important for Coandă UAVs due to the coupling of the different variables that contribute to its special aerodynamics. However, although the Coandă effect is well-known, its control has not been yet sufficiently explored in the existing literature.

The hypothesis of this work is whether the innovative mechatronic design of the Coandă effect UAV, characterized by structural adjustments, manufacturing with strategic materials and experimentation with air channeling, directly impacts the effectiveness and performance of the implemented control algorithms. We propose that the relationship between physical design and control algorithms goes beyond the mere standard implementation of fuzzy logic and PID. We hypothesize that unique design features, as well as air channeling and flap coordination, significantly influence the drone's response to control commands. In addressing this hypothesis, our goal is not only to demonstrate the uniqueness of our mechatronic design, but also to underline the essential interconnection between the physicality of the Coandă effect UAV and the innovation in control algorithms.

The purpose of this paper intended two significant contributions: (1)

* Corresponding author.
E-mail address: tomas.mateo@diesia.uhu.es (T.J. Mateo Sanguino).

https://doi.org/10.1016/j.robot.2024.104662
Received 2 June 2023; Received in revised form 15 January 2024; Accepted 11 February 2024
Available online 18 February 2024

Nomenclature

A	area of the UAV surface
$accData$	value from the accelerometer sensor
acc_x	value for the accelerometer in the X axis
acc_y	value for the accelerometer in the Y axis
a_{global}	acceleration in the global coordinate system
a_{UAV}	acceleration in the UAV coordinate system
$Ae(t)$	inclination error as a function of time
$Angle$	value to compute (i.e., pitch or roll depending on the case)
α_{UAV}	angular acceleration
Δt	time since the last calculation of the filter
B	volume of a system
d	vertical distance between CG and flaps
$deflex_n$	flap deflections for the n-side
$error_z$	difference between measured height and reference height
F_i	force on a plane
F_{flap}	reaction force at a flap
F_{global}	forces in the global coordinate system
F_{net}	net force or lift force
F_{sur}	force on the Coandă surface
g	acceleration due to gravity
$gyrData$	angle from the gyroscopic sensor
γ	angle of a flap
h	UAV elevation above a reference plane
k	multiplying factor
K_{eff}	flap efficiency
Kp	proportional constant for velocity
kp_{angle}	proportional constant for angle
m	mass of a system
M_i	reaction torque and antitorque
n	normal vector of a control surface
P_{bat}	power expressed in Wh
p_i	pressure in Pascal under and above the UAV
$pitch$	angular value for the Y axis
p_{net}	net pressure of the system
PWM_{max}	PWM signal at full range
PWM_{motor}	PWM signal for the hovering condition
P_{UAV}	power consumed by the system
r_i	horizontal distance from CG to a flap
R_{xyz}	rotation matrix
$roll$	angular value for the X axis
ρ	density
T_{bat}	battery endurance
T_m	thrust of the brushless motor
td	derivative constant for velocity
ti	integrative constant for velocity
φ	horizontal distance between CG and flaps
Φ, θ, ψ	rotation of the UAV
μAnd	minimum value of implication and conjunction
$\mu Prod$	T-norm of the product
$\mu(x_i)$	membership value in the universe of the rule consequent
v	velocity of a system
V	volume of a system
$Ve(t)$	angular velocity error as a function of time
v_i	airflow velocity at the UAV bottom and top
W_e	weight of the electronics
W_m	weight of the brushless motor
W_s	weight of the mechanical structure
ω	angular velocity
XYZ	position of the UAV
x_i	point in the universe of the rule consequent
Z	measured height

to improve previous Coandă systems developed according to cost, sensing, communication and flight control software, and (2) to examine the applicability of a Fuzzy logic controller (FLC) in a Coandă-based UAV to takeoff, stabilize and land. To achieve these goals, the paper covers the design and construction of the mechatronics for this special class of aircraft, including simulation verification and flight test results to demonstrate the methodology employed in implementing the UAV. Therefore, the paper is structured as follows. Section 2 provides a comprehensive literature review of the state of the art and the control of similar solutions. Section 3 gives a brief introduction on the physics of the Coandă effect and the theoretical analysis. Section 4 discusses the innovative design and development of the Coandă UAV including materials for the manufacturing, electronics, sensors, and actuators for the subsequent intelligent control. Section 5 provides a detailed explanation on the PID and Fuzzy logic controllers developed. Section 6 discusses the experimentation. Finally, Section 7 presents the conclusions and future works.

2. State of the art

The first application of the Coandă effect was *Aerodyne Lenticulaire* in 1935, a hovercraft very similar in shape to a flying saucer. This was later improved in Germany during WWII by means of twelve Junkers Jumo 004B jet engines radially installed at the edge of a 20 m diameter disc [7]. Coandă's research was validated by the US during postwar, thus leading to the VZ-9-AV aircraft, a proof-of-concept project jointly developed with Canada by Avro Aircraft Ltd. in 1958 as part of a series of military developments. This VTOL design, nicknamed *Avrocar*, intended to improve the performance of its German antecessor by employing a single turbo-rotor and three Continental J69-T-9 turbojet engines [8]. Meanwhile in the US, Lockheed Corp. and Convair Corp. tested several experimental saucer-shaped crafts with the advantages of the VTOL designs and a shape suited to diffuse RADAR signals [9].

It was not until 2002 when the Coandă effect was again publicly applied simultaneously in two aerial vehicles by R. Collins [10] and G. Hutton [11] in UK, thus resulting in new patents. In this manner, the circular shape became octagonal with anti-torque side rudders and steering flat flaps on opposite sides at the bottom of the fuselage to gain stability [11]. This was followed by other similar designs such as the GFS-UAV N-01A model, a radio-controlled Coandă UAV propelled by an electric brushless motor [12]; the ring wing airfoil concept, a mockup devised to investigate the use of the Coandă effect in novel UAVs [13]; Fantail 5000, a VTOL aircraft from ST Aerospace powered by a 3.5 HP gasoline engine [14]; MEDIAS, a non-polluting UAV for environmental monitoring equipped with a helium inflatable chamber able to increase its autonomy [15]; RQ-16 T-Hawk, a ducted fan UAV made by Honeywell that thrusts more efficiently than using an open rotor or propeller for the same diameter and equivalent power [16]; Embla, an optimized design made by AESIR Ltd. that improved the airflow over the outer surface to gain stability under lateral wind [17]; Vidar, a battery-powered UAV of 300 mm in diameter constructed by AESIR Ltd. to carry small payloads (~100 gr) in cluttered environments (e.g., buildings) during 15 min of autonomy [18]; Odin, a 1m-diameter UAV, also by AESIR Ltd., powered by a rotary JP-8 internal-combustion engine capable of carrying medium-weight payloads (~10 Kg) during 60 min [18]; Hoder, a variant of double-rotor UAV capable of carrying up to 1-tonne payload for military cargo transport during 8 h [18]; a vertical/short-TOL aircraft, a version fitting a lift system that requires no external moving parts and reduces aerodynamic losses thanks to an annular wing wrapped around a wind-turbine generator [19]; Anuloid,

an innovative disk-shaped VTOL aircraft that includes several key features (i.e., ducted fan and control vanes) to improve the static performance and dynamic stability [20]; a two-rotor VTOL aircraft from Khulna University of Engineering & Technology (KUET) designed with two type of flaps and rudders that makes it more maneuverability against impacts than conventional unmanned planes [21]; a small-scale Coandă UAV from Sharif University of Technology in Teheran, Iran for which a FFT-based motion disturbance analysis was proposed to evaluate its mechanical design and development [22]; and SCoandă, an UAV for which the equations of the dynamic model were obtained to simulate a PID-based flight controller [23].

Current research is focused on optimizing Coanda surface design for UAVs, particularly exploring novel configurations for enhance thrust/lift performance. This is the case of two studies that used linear rectangular and straight cylindrical surface arrangements to improve performance by 17% to 45%, respectively [24–25]. Moreover, the Coandă effect is also being tested nowadays in helicopters with no tail rotor as in NOTAR [20–26] or in spherical drones propelled by closed impellers utilizing the Coanda effect [27]. The benefit of using the Coandă effect with a single rotor also effectively reduces noise, offering a potential breakthrough for acoustical stealth in drone operations compared to conventional multi-rotor systems [28]. Current use of single rotors includes other hybrid concepts like Gimball, a small ultralight flying spheroid robot —34 cm in diameter and 370 gr— that can operate in extremely chaotic environments without the need for fragile sensors [29] or the integration of fixed-wing and rotary-wing elements in a Coanda-drone that proposes improving system force through four thrusters [30].

In this context, the paper addresses the design and construction of a small UAV based on the Coandă effect developed at the University of Huelva (Spain). To introduce the UAV, its main features and properties are compared in Table I. It includes several innovative features in its mechatronic design. The scaled reduction and fixed side rudders, inspired by established principles, enhance maneuverability while minimizing weight, complexity, and cost. The integration of Balsa wood in the internal structure ensures a fine balance between strength and weight. The propulsion system, comprising a brushless DC motor and optimized carbon fiber propeller, ensures efficient and reliable performance. The experimental determination of optimal air channeling using various duct configurations is distinctive to our design, with the cylindrical Depron duct emerging as the most effective. Additionally, the incorporation of servos for precise control of flaps adds a layer of stability to the UAV. The hardware system –based on an Arduino NANO microcontroller– supports a range of electronic components, including redundant ultrasonic sensors for ground proximity measurement. The software system, programmed in C++ through Arduino IDE, enables faster and more robust responses in uncertain environments. It served to further develop a Fuzzy logic controller and a graphical user interface (GUI). To the best of our knowledge, this research is the first time it has been addressed for a Coandă Effect-based UAV.

2.1. Works related to systems control

Airplanes based on the horizontal take-off and landing (HTOL) typically require simpler control than the UAVs based on the vertical take-off and landing (VTOL). However, HTOL generally offers lower maneuverability and dismisses the autonomy due to the higher number of engines, thus being highly dependent on energy accumulators [31].

The fine tuning of parameters and features for the flight control of an UAV is a critical task due to the non-linear aircraft characteristics [32]. Classical PID controllers have many benefits and have been used in drones with Coandă effect [23–27]. Nonetheless, the setup process of the system is pretty difficult because of the dynamics, which becomes even more complicated when they present lateral and longitudinal elements (e.g., altitude, speed and heading inputs for the elevator deflection, throttle, pitch angle/rate, aileron and roll attitude/rate outputs) [33]. To make this process easier, several Fuzzy logic controllers (FLC) have been applied to classical planes and multi-rotor UAVs. For example, a hybrid Fuzzy logic and adaptive control was developed to stabilize and operate a fixed-wing UAV called Aerosonde [34]. Similarly, a FLC was

Table 1
Comparison of features and capabilities for various UAVs designed for military and civil missions.

Name	Aerodynamics	Engine	Sensors	Control System	COMM System	Software	Material	Weight (Kg)	Cost	Mission	Year
Aerodyne L.	Coandă	12x Turbojet	No	Obturator	No	No	Metal	High	High	Military	1944
Avrocar	Coandă	3x Turbojet	✓	Gyroscopic	No	No	Steel	1361	High	Military	1958
R. Collins	Coandă	DGT	External	Actuators	No	No	Al/Balsa	~1.0	Mid.	Civil	2002
Parafoil*	Wind	No	GPS	FLC/GA	No	Matlab/Simulink	–	–	–	Military	2005
GFS-UAV	Coandă	BLDC	No	Actuators	RC	No	Wood/EPS	0.533	Mid.	Civil	2006
Fantail 5000	Duct fan	GAS	✓	GPS	RC	Windows-GCS	CF	5.5	High	Military	2006
MEDIAS	Coandă	BLDC/He	No	No	No	No	FG/Balsa	2.8	Low	Civil	2008
T-Hawk	Duct fan	GAS	✓	MEM	RC	Windows-GCS	CF	8.4	High	Military	2008
Embla	Coandă	BLDC	✓	Actuators	RC	Onboard camera	CF	0.4	High	Military	2009
Hoder	Coandă	2x BLDC	✓	Actuators	RC	N/A	CF	1500	High	Military	2009
Aerosonde*	FWA	No	✓	FLC/MRAC	No	Simulink/Aerosim	–	–	–	Civil	2011
Tiger 60	FWA	GAS	✓	FLC/GPS	RC	AirGuardian	Balsa/ Plywood	4.0	Mid.	Civil	2012
Odin	Duct fan	Jet fuel	✓	AFCS	RC	Windows-GCS	CF	10	High	Military	2013
Gimball	Thrust	BLDC	✓	Gyroscopic	RC	Onboard camera	Plastic	0.370	Mid.	Civil	2013
Quad*	Thrust	4x BLDC	No	FLC	No	Matlab/Simulink	–	–	–	Civil	2014
Anuloid*	Ducted Coandă	Turboshaft	No	No	No	Patran/Nastran/ EDGE/ ANSYS	CFRP	1200	–	Civil	2014
KUET	Coandă	2x BLDC	No	No	No	No	Foam	~1.5	Low	Civil	2015
Sharif	Coandă	BLDC	✓	No	RC	No	EPS	1.6	Low	Civil	2015
SCoandă	Coandă	BLDC	✓	PID	RC	No	CF	1.05	Low	Civil	2017
SpICED	Coandă duct fan	8x BLDC	✓	PID	WiFi	Turbomachinery	Foil & helium gas	0.298	Low	Civil	2022
UHU	Coandă	BLDC	✓	FLC	Bluetooth	Matlab/LabVIEW	Balsa/XPS	1.46	Low	Civil	2023

* = Simulated; AFCS = Automatic flight control system; Al = Aluminium; BLDC = Brushless DC motor; CF = Carbon fiber; CFRP = Carbon fiber reinforced polymer; COMM = Communication; DGT = Disk gas turbine; EPS = Expanded polystyrene; FB = Fiberglass; FLC = Fuzzy logic controller; FWA = Fixed-wing aircraft; GA = Genetic algorithm; GAS = Gasoline; GCS = Ground control station; He = Helium; MEM = Microelectromechanical; MRAC = Model Reference Adaptive Control; RC = Radio controlled; N/A = Not available; XPS = Extruded polystyrene.

designed for the AERObot autopilot of a fixed-wing UAV —called Tiger 60— with better performance than classical controllers [35]. Also, a FLC for the control of the height, roll, pitch and yaw inputs was designed to simulate a quad rotor model [36]. Finally, [37] shows how to optimize the Fuzzy rules with a steady state genetic algorithm to fly a small autonomous parafoil.

3. Theoretical analysis

The Coandă effect of fluid dynamics was discovered in 1936 by Henri M. Coandă, a Romanian inventor (1886–1972), who published two first patents describing its application [38–39]. The aerodynamic Coandă effect is generated when a high-velocity airflow is expelled tangentially into an adjacent surface and remains attached along its curved shape within the limits of an angle of attack. Applied to aircrafts, the Coandă effect is obtained by an upper rotor that entrains an airflow from the surroundings towards an inverted bowl shape through a duct. This creates a difference of pressures due to the higher velocity of the airflow through the circular slit between the rotor duct and the surface (i.e., low pressure vortex), and the lower velocity of the air below the bowl (i.e., higher pressure environment). Fig. 1 provides a visual illustration of the prototype that links the problem statement described and subsequent system images (Fig. 2 and 3). Such illustration is intended to help understand the mathematical model presented in Section 3, particularly with respect to quantities such as force and airflow velocity that require inertial or moving references.

3.1. Bernoulli's principle

Following the principle of D. Bernoulli (1700–1782) that relates pressure, kinetic energy, and gravitational energy, this can be mathematically described as follows:

$$p_1 + \frac{1}{2}\rho v_1^2 + \rho g h = p_2 + \frac{1}{2}\rho v_2^2 + \rho g h \tag{1}$$

where p_1 and p_2 are the pressures in Pascal under and above the UAV respectively, ρ is the air density expressed in Kg/m^3 at all points in the fluid, which does not change with pressure (i.e., the air remains incompressible), v_1 and v_2 stand for the airflow velocity in m/s at the bottom and the top respectively, g is the acceleration due to gravity and h is the elevation above a reference plane.

The difference between the top and the bottom in terms of gravitational potential energy ($\rho g h$) can be considered smaller than the other terms in Eq. (1). Therefore, a simplified form of the equation can be obtained after omitting and rearranging the terms as follows:

$$p_1 - p_2 = \frac{1}{2}\rho\left(v_2^2 - v_1^2\right) \tag{2}$$

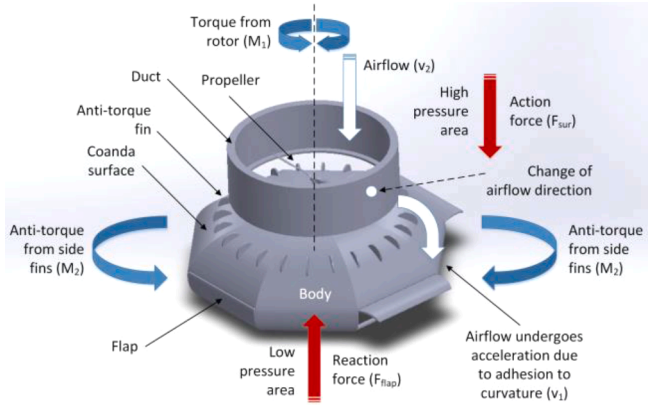

Fig. 1. Proposed proptotype and aerodynamic effect.

$$(p_1 - p_2)A = p_{net}\cdot A = \mathrm{F_{net}} \tag{3}$$

where A stands for the area of the UAV surface in m^2, p_{net} is the net pressure of the system and $\mathrm{F_{net}}$ is the net force or lift force expressed in Newtons. This effect favors the aerodynamic sustenance of the UAV due to the difference of pressures causing a vacuum on the top, which pushes the aircraft upwards thanks to the downward thrust of the engine according to the Newton's third law [13].

3.2. System forces

The forces acting on the flaps by the airflow determine the translational motion of the UAV along the X and Y axes. From the Newton's fundamental law of mechanics, such forces can be related with the mass and velocity of the system through the following mathematical reasoning:

$$\mathrm{F_{net}} = ma = m\frac{\mathrm{d}v}{\mathrm{d}t} \tag{4}$$

$$\mathrm{F_{net}} = \frac{\mathrm{d}}{\mathrm{d}t}(mv)_{\mathrm{sys}} \tag{5}$$

From the Reynolds transport theorem, any property of an object ($B = mv$) is the intensive property associated with a small portion of the object ($\mathrm{d}B/\mathrm{d}m = \beta$). So, according to Eq. (5):

$$\frac{\mathrm{d}}{\mathrm{d}t}B_{\mathrm{sys}} = \frac{1}{\mathrm{d}t}\left[\int_{\mathrm{CV}}\beta\mathrm{d}m\right] + \sum_{i=0}^{n}(\beta_i \mathrm{d}m_i)|_{\mathrm{out}} - \sum_{i=0}^{n}(\beta_i \mathrm{d}m_i)|_{\mathrm{in}} \tag{6}$$

where the property of a system (i.e., momentum) is considered as the property of each mass differential of an arbitrary control volume (CV) and a control surface through which the property acts (i.e., in and out). Given the density of an object as defined in Eq. (7), the previous expression can be conveniently formulated as follows:

$$\rho = \frac{m}{v} \tag{7}$$

$$\frac{\mathrm{d}}{\mathrm{d}t}B_{\mathrm{sys}} = \frac{1}{\mathrm{d}t}\left[\int_{\mathrm{CV}}\rho v(\mathrm{d}V)\right] + \int_{\mathrm{cs}}\rho v(Vn)\mathrm{d}A \tag{8}$$

where V means the volume of the CV, A stands for the area of the control surface (CS) and n is the normal vector of each CS. We conveniently locate CV on a flap to equate the momentum of each differential mass with the momentum of each particle in a fluid (i.e., airflow that enters and exits). Then, the first term of the previous expression can be removed as the airflow through CV is stable. Thereby, Eq. (5) can be simplified through Eq. (6) as follows:

$$\mathrm{F_{net}} = \int_{\mathrm{cs}}\rho v(Vn)\mathrm{d}A \tag{9}$$

$$\mathrm{F_{net}} = \sum_{i=0}^{n}(\mathrm{d}m_i v_i)|_{\mathrm{out}} - \sum_{i=0}^{n}(\mathrm{d}m_i v_i)|_{\mathrm{in}} = -\mathrm{F_{flap}} \tag{10}$$

In brief, the translational motion of the UAV is produced by a sum of forces, whose airflow on the flaps produces a reaction force named $\mathrm{F_{flap}}$. Therefore, $\mathrm{F_{flap}}$ is proportional to the force on the Coandă surface ($\mathrm{F_{sur}}$):

$$\left|\mathrm{F_{flap}}\right| = K_{eff}\cdot|\mathrm{F_{sur}}| \tag{11}$$

$$\left|\mathrm{F_{flap}}\right|_{\mathrm{x,y}} = K_{eff}\cdot|\mathrm{F_{sur}}|\cos\gamma \tag{12}$$

$$\left|\mathrm{F_{flap}}\right|_{\mathrm{z}} = K_{eff}\cdot|\mathrm{F_{sur}}|(1-\sin\gamma) \tag{13}$$

where K_{eff} is the flap efficiency and γ stands for the angle of a flap under the assumption that the airflow enters the CV parallel to the Z-axis of a flap. In that way, $\mathrm{F_1}$ and $\mathrm{F_3}$ are a couple of forces defined on the XZ

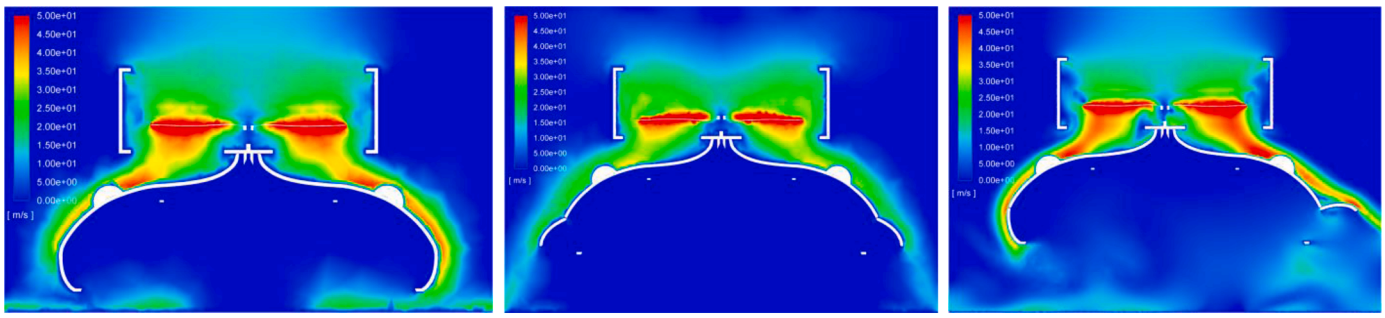

(a) (b) (c)

Fig. 2. Airflow velocity for the proposed UAV analyzed through computational fluid dynamics: (a) flaps at 0°, (b) flaps at 45°, and (c) flaps at 0 and 90°.

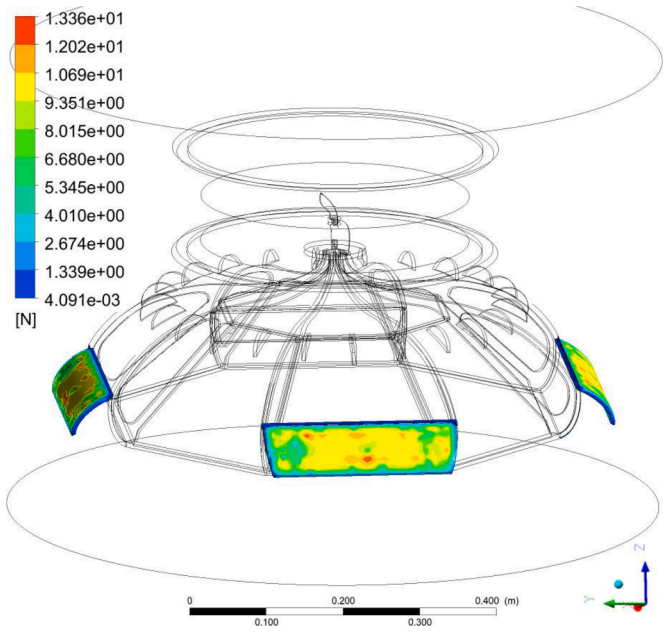

Fig. 3. Force model on the flaps of the UAV analyzed with computational fluid dynamics.

plane, whilst F_2 and F_4 are couples on the YZ plane.

Accordingly, the sum of forces to lift the Coandă UAV along the Z-axis must overcome the gravity (g) with an airflow acting on eight surfaces and four flaps:

$$\mathbf{F_{net|z}} = 8\mathbf{F_{sur}} + 4\mathbf{F_{flap|z}} = m\mathbf{g} \tag{14}$$

Including Eq. (13) into Eq. (14), this requires a minimum force to lift with $F_{sur} = 2.0614$ N considering a weight of $m = 1460$ gr., K_{eff} of 0.9 and γ set at 45° for the flaps in idle position. We obtained a maximum force of $F_{sur} = 13.36$ N with an airflow velocity of 50 m/s produced by the blades turning at 12,100 r.p.m. To validate the results, Fig. 2 shows the airflow velocity in different flap configurations obtained through computational fluid dynamics (CFD) with Ansys Fluent®, while the maximum force (F_{sur}) obtained with flaps at 45° for such airflow velocity is shown in Fig. 3.

3.3. System dynamics

According to Newton's second law, the forces acting on the UAV with respect to the global coordinate system is as follows:

$$F_{global} = ma_{global} = R_{xyz}ma_{UAV} - mg \tag{15}$$

where a_{global} is the acceleration acting on the UAV with respect to the global coordinate system, a_{UAV} is the acceleration acting on the UAV in the local coordinate system and R_{xyz} is the rotation matrix. As the vehicle rotates on the XYZ axes by the Φ, θ and ψ Euler angles, the rotation matrix R_{xyz} included in Eq. (15) is defined in the following form:

$$R_{xyz} = f(\phi, \theta, \psi) \tag{16}$$

$$R_{xyz} = \begin{bmatrix} c\psi c\theta & c\phi s\psi + c\psi s\phi s\theta & s\phi s\psi - c\phi c\psi s\theta \\ -c\theta s\psi & c\phi c\psi - s\phi s\psi s\theta & c\psi s\phi + c\phi s\psi s\theta \\ s\theta & -c\theta s\phi & c\phi c\theta \end{bmatrix} \tag{17}$$

Therefore, the XYZ position of the UAV in the global coordinate system is calculated as follows:

$$\begin{bmatrix} X & Y & Z \end{bmatrix}^{T} = \int\int \left[R_{xyz}a_{UAV} - g\right]dt \tag{18}$$

The linear acceleration acting on the UAV (a_{UAV}) with respect to the global coordinate system is then obtained from Eq. (15):

$$\frac{F_{global}}{m} = a_{global} = R_{xyz}a_{UAV} - g \tag{19}$$

As defined in Eq. (4), the sum of forces acting on the system is that force acting on the UAV with respect to the global coordinate system:

$$a_{global} = R_{xyz}\cdot\frac{F_{net}}{m} - g \tag{20}$$

Since F_{net} is defined through Eq. (10) to Eq. (13), the linear acceleration acting on the UAV can be conveniently arranged:

$$a_{global} = \frac{-F_{sur}}{m}\begin{bmatrix} \left\{ \begin{matrix} K_{eff}c\psi c\theta(c\gamma_1 - s\gamma_1) + K_{eff}(c\gamma_2 - s\gamma_2) \\ (c\phi s\psi + c\psi s\phi s\theta) - (s\phi s\psi - c\phi c\psi s\theta)P \end{matrix} \right\} \\ -\left\{ \begin{matrix} K_{eff}c\theta s\psi(c\gamma_1 - s\gamma_1) - K_{eff}(c\gamma_2 - s\gamma_2) \\ (c\phi c\psi - s\phi s\psi s\theta) + (c\psi s\phi + c\phi s\psi s\theta)P \end{matrix} \right\} \\ \left\{ \begin{matrix} K_{eff}s\theta(c\gamma_1 - s\gamma_1) + K_{eff}c\theta s\phi(c\gamma_2 - s\gamma_2) \\ +c\phi c\theta P \end{matrix} \right\} \end{bmatrix} - \begin{bmatrix} 0 \\ 0 \\ g \end{bmatrix} \tag{21}$$

where $P = K_{eff}\,c\gamma_1 - 4K_{eff} + K_{eff}\,c\gamma_2 + K_{eff}\,s\gamma_1 + K_{eff}\,s\gamma_2 + 8$.

Moreover, the angular position of the UAV along the XYZ axes can be related with the angular motion of the system. To this end, the moment of force of the UAV with respect to the center of gravity (CG) is utilized according to Newtonian mechanics:

$$\tau_{UAV} = \begin{bmatrix} r_2\cdot F_2 + r_4\cdot F_4 \\ r_1\cdot F_1 + r_3\cdot F_3 \\ M_2 - M_1 \end{bmatrix} \tag{22}$$

where r_1, r_2, r_3 and r_4 are the horizontal distances from CG to the action

point of each force at the flaps, and M_1 and M_2 are the reaction torque and antitorque produced by the side fins. The subtraction is ideally zero when adjusted.

The moment of force on a body determines the rate of change of the UAV`s angular momentum (L):

$$\tau_{\mathrm{UAV}} = \frac{d\mathrm{L}}{dt} = \frac{dI\omega}{dt} = I\alpha_{\mathrm{UAV}} \tag{23}$$

where I stands for the moment of inertia, ω is the angular velocity and α_{UAV} is the angular acceleration. The rotation of the UAV on the XYZ axes by Φ, θ and ψ is then calculated when integrated about time as follows:

$$[\phi \quad \theta \quad \psi]^{\mathrm{T}} = \int\int \alpha_{\mathrm{UAV}} dt \tag{24}$$

From Eq. (22) and Eq. (23), the angular acceleration acting on the UAV can be conveniently arranged:

$$\alpha_{UAV} = \begin{bmatrix} \left\{ -\mathrm{F}_{\mathrm{sur}} K_{eff} (\mathrm{c}\gamma_2 - \mathrm{s}\gamma_2) \left(d + \frac{\varphi}{2}\right) \Big/ I_{11} \right\} \\ \left\{ \mathrm{F}_{\mathrm{sur}} K_{eff} (\mathrm{c}\gamma_1 - \mathrm{s}\gamma_1) \left(d + \frac{\varphi}{2}\right) \Big/ I_{22} \right\} \\ \{(\mathrm{M}_1 - \mathrm{M}_2)/I_{33}\} \end{bmatrix} \tag{25}$$

where d is the vertical distance between CG and the flaps on the Z axis, and φ is the horizontal distance between CG and the flaps on the X and Y axes (i.e., diameter). The moment of inertia about CG was calculated through CFD simulation with Ansys Fluent®, for which we obtained a maximum value of 0.0067 kg·m^2 at the pivot of the flaps.

4. Mechatronic system design

The design approach of our UAV followed the design from [11–12] with a scale reduction of 0.62 and fixed side rudders. These adjustments resulted in a lower weight, complexity, and cost of the prototype at the expense of a more accurate flight control. Its internal structure was entirely constructed with Balsa wood (i.e., *Ochroma pyramidale*) —typically used in aeromodelling— due to its fine properties. This is characterized by a soft and very light material, easy to handle, with large strength-to-weight ratio. The total process consisted in the following tasks: *i*) design of the whole structure; *ii*) search and collect of construction materials; *iii*) cut and sand of parts; *iv*) assemble of the structure; *v*) finish the fuselage with rudders and flaps; *vi*) place the engine on platform; *vii*) place the sensors and actuators on the UAV; and *viii*) place the top duct. The various parts of the framework were glued with Cyanoacrylate and Epoxy paste to provide the elasticity and strain required by the joins (i.e., up to 30 MPa). The wooden skeleton was then coated with Depron, a white extruded polystyrene sheet (i.e., 6 mm thick and 30 Kg/m^3 of density) easier to handle and lighter compared with the Balsa wood (Fig. 4).

The brushless DC motor was fixed through a circular piece of wood and four metal threaded rods, which used a 13 × 4 carbon fiber propeller by Quanum. The air channeling of the UAV through the nozzle was experimentally measured as described in [40]. To this end, we tested different configurations as for instance a cylindrical polypropylene duct of 150 g, a conic polypropylene duct of 350 g, a cylindrical Depron duct of 70 g, and a cylindrical cardboard duct of 100 g with height slits of 3.5 cm, 7.5 cm and 10 cm, respectively. After testing, the optimal configuration found consisted of the cylindrical Depron duct of 70 g with a gap of 7.5 cm. In addition, we used two servos to control the four flaps in charge of providing the stability and flight direction of the UAV. This was possible through a crankshaft mechanism in which the end attached to a servomotor was joined to the flaps through a connecting rod and a piston. In that way, when a flap was positioned at an opening angle whilst the opposite flap was set in an inverted position, a difference of pressure —and fluid velocity— was created in opposite sides of the UAV. This causes the Coandă UAV to turn to where the airflow has less velocity.

4.1. Hardware system

The electronic components were attached on the center axis of the UAV's interior body to favor the payload balance. The hardware system was based on an Arduino NANO microcontroller. It was selected due to its small size and weight in relation to its features (18 × 45 mm^2 of size, 7 g of weight and 19 mA of power consumption at 5 V). The engine consisted of a Turnigy 3639 brushless motor 1100kv (max. peak current of 30–45A/20S at 11.1 V). This item was chosen instead of the brushed motors due to the less maintenance because of the lack of brushes, better heat dissipation, higher speed range and lower EMI noise. As main disadvantage, it required a three-phase voltage generated by an electronic speed controller (ESC) through a PWM signal at the

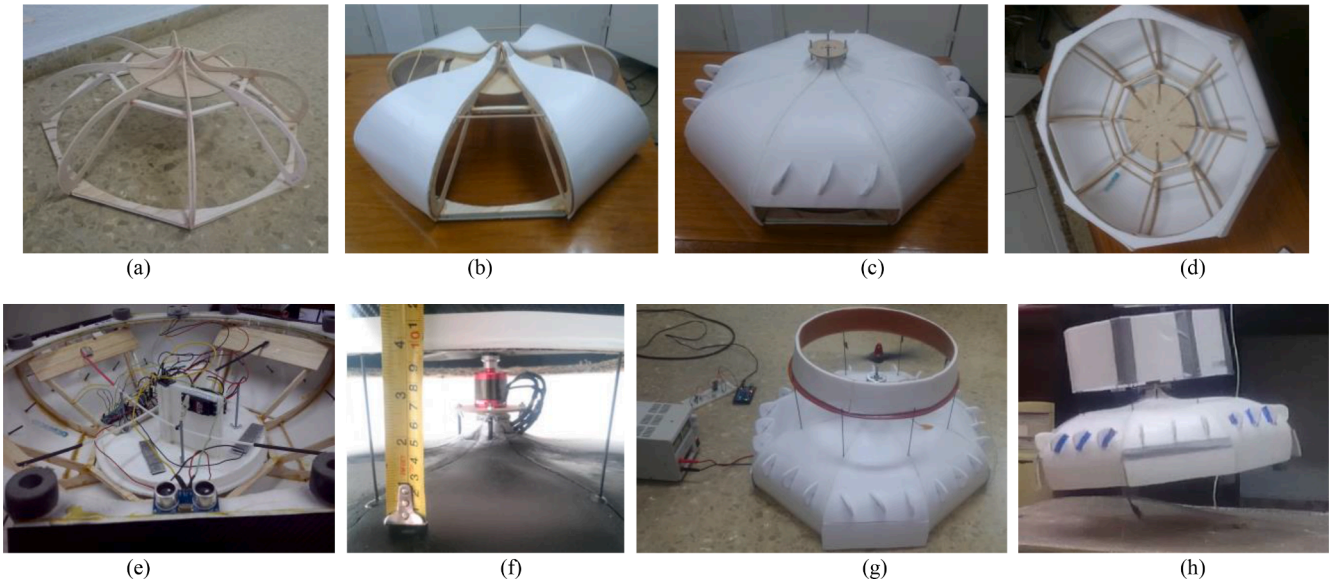

Fig. 4. Mechanical construction of the Coandă UAV: (a) skeleton, (b) construction of the fuselage, (c) exterior view of the curved surface, (d) internal view of the structure, (e) detail of the internal electronics, (f) detail of the slit around the BLDC motor, (g) test with the ducted fan, and (h) elevation in the air.

microcontroller. This consisted in a 50 Hz signal generated by a Turnigy AE-80A brushless ESC with an activation pulse between 1 ms and 2 ms. Following Eq. (26), the thrust of the brushless motor (2150 g) was sized according to Table 2 and therefore suitable for the UAV weight (1460 g).

$$T_m \geq W_m + W_s + W_e \tag{26}$$

We also used two HS-5585MH servos from HITEC to control the position of the flaps. As for the inertial measurement unit, we used a GY-85 IMU of nine degrees of freedom provided by an ITG3200 gyroscope (12 bits), an ADXL345 accelerometer (13 bits) and a HMC5883L magnetometer (16 bits). We also used two redundant HC-SR04 ultrasonic sensors to measure the range of the UAV above the ground. The energy of the system was provided by a Rhino 2250 mAh Li-Po pack (3S2P 11.1 V, 25C). This battery was selected due to its better performance regarding the recharging time, life cycle and energy density in relation to the Ni-Cd, Ni-Mh or Li-Ion batteries. To adapt the power requirements, we used a 25 W step-down power supply converter (90% efficiency) from CPT. Considering the consumption of the microcontroller, the brushless motor and the servos in Eq. (27), it resulted in ~4.45 min of autonomy at maximum load (Table 3).

$$T_{bat} = \frac{P_{bat}}{P_{UAV}} \text{x} \frac{60\text{min}}{1\text{hour}} = 4.45\text{min} \tag{27}$$

Alternatively, a lead acid battery (12 V, 40A) was used in laboratory tests for long-term purposes, thereby increasing the autonomy to ~85.56 min. A complete diagram depicting the hardware of the system can be found in Fig. 5. The cost of the whole UAV platform —regardless of the navigation and monitoring software— was US $600.

4.2. Software system

The microcontroller unit was programmed with the Arduino IDE using the C++ language. The main function of its software was to initialize and calibrate the electronics, send data from the sensors, update the sensor readings, and control the actuators (i.e., the BLDC motor speed, X and Y positions of the servos and IMU calibration). These parameters were transmitted between the Arduino microcontroller and the GUI through AT commands thanks to a HC-05 Class 2 Bluetooth® module from BricoGeek® capable of communicating up to 2.1 Mbps. Despite of its short range —up to 10m— the distance coverage was increased with a high gain antenna. It was selected due to its good response against interferences (i.e., sensitivity ≤ -84 dBm at 0.1% BER).

The GUI was developed in LabVIEW™ 2011 and tested with an Intel Core i7 (2.6 GHz, 16-GB RAM). The aim of this application was to remotely control and monitor the UAV parameters. The readings consisted of the BLDC motor speed, pitch, yaw and roll, flight height, electronics temperature, and time. For greater ease, a set of shortcuts were included to control the functions of the UAV by means of the buttons and the analog joysticks of a Saitek P880 pad (i.e., accelerate the BLDC motor, lift the UAV at slow, medium or maximum speed, change the UAV direction, and stop the UAV). This facilitated the manual control through a virtual instrument at the GUI in which the data were showed in real time through digital displays, charts, and 3D graphs [41].

Table 2
Bill of mechanics & electronic devices.

Name	Units	Weight (g)	Total Weight (g)
Structure of Balsa/XPS	1	550	550
Air duct	1	30	30
Paddle rod	2	5	10
Rudder rod	4	10	40
Support for electronics	2	25	50
HC-SR04 sensor	2	7	14
GY-85 IMU	1	1	1
HC-05 Bluetooth module	1	3	3
DC/DC converter	1	65	65
HS-5585MH servo	2	60	120
BLDC motor	1	136	136
Li-Po battery	1	352	352
Brushless ESC	1	72	72
Mechanical structure (W_s)	–	–	680
Electronics (W_e)	–	–	645
BLDC motor (W_m)			136
Total UAV	–	–	1460

Table 3
Consumption of the electronics at maximum power.

Name	Voltage (V)	Current (mA)	Power (W)
2x HC-SR04 sensor	5	30	0.15
GY-85 IMU	5	6.62	0.0031
HC-05 Bluetooth module	5	40	0.2
2x HS-5585MH servo	5	80	0.4
BLDC motor	11.1	30,000	330
Arduino microcontroller	5	560	2.8
Total electronics (P_{UAV})	–	–	336.5831

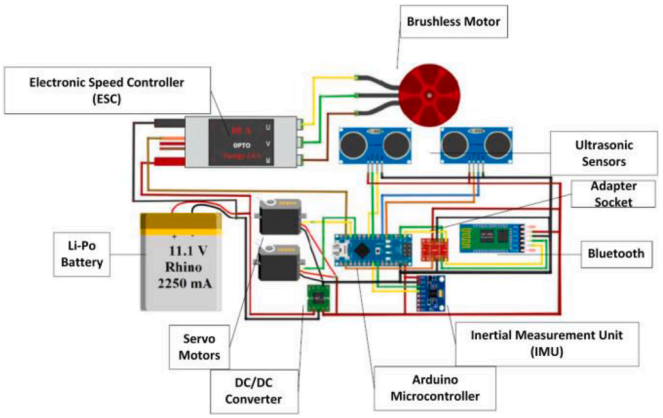

Fig. 5. Conection of the electronics of the UAV.

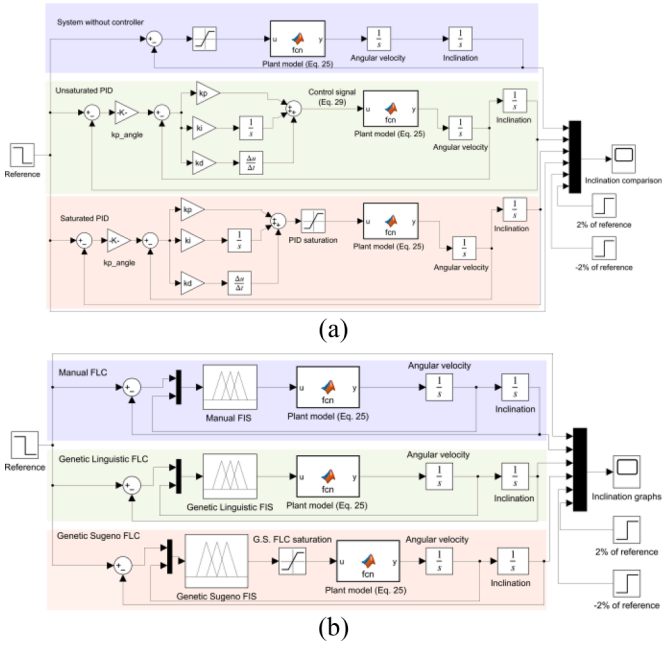

Fig. 6. Comparison of studied models in Simulink: (a) system without controller, unsaturated and saturated PID controllers, and (b) manual, genetic Mandani and genetic Sugeno controllers. FIS = Fuzzy Inference System.

5. Dynamic system control

In order to validate the system dynamics controllers, a test bench has been designed in Simulink (Fig. 6). It has been divided into two schematics to ease the graphic representation (Fig. 6a and Fig. 6b). The objetive of this test bench is to calculate the settling time, overshoot and position error of each of the controllers applied to the UAV. This is performed by selecting an initial angle, a target angle, and then measuring the response of each controller.

5.1. PID controller

Fig. 6a includes the flight control system without any controller (purple background), which is useful to compare the plant's behaviour against the other models. In this case, the inclination error is the input and the current inclination of the model is the output. This is obtained after performing a double integral from the angular acceleration in the Laplace domain, the latter being the output of the UAV plant.

To stabilize the roll and pitch of the UAV (i.e., X and Y axes), a PID approach has been designed using the UAV plant model described in Section 3C (Eq. (25)), which represents the angular acceleration of the UAV. The plant model is located at the output of the PID controller, to which two integration blocks are applied in the Laplace domain to obtain the angular velocity and inclination of the UAV. The PID parameters have been adjusted experimentally by an expert system, whose values are listed in Table 4. Firstly, a PID controller without restriction of the maximum opening angle of the flaps is studied for comparison purposes (i.e., called unsaturated PID in Fig. 6a, green background). In this case, the inclination error combined with the angular velocity is the input to the PID controller. That way, the opening angle of the flap is calculated by the PID controller. Secondly, a PID controller with a plant model restricted to $\pm 45^{\circ}$ is included (i.e., called saturated PID in Fig. 6a, orange background). This limitation is necessary due to the real maximum and minimum opening angles that the UAV flaps can take. The input of this PID controller is the same as for the previous case.

Each of the PID controllers consists of a double loop (Eq. (28)). The first one is used as a proportional controller to achieve the target angle (i.e., 'kp_angle' in Fig. 6a), whose output is taken as input for the second PID. Its input is the error calculated between the target angle and the current inclination angle. The second one is responsible for controlling the rotation velocity of the UAV on the X and Y axes. This input is the error calculated between the output of the first loop and the current angular velocity of the UAV. For our case study, the derivative part has not been used in the PID controller (i.e., represented by zero value) since it increases the settling time, produces noise in the control signal and slows down the system transient. This causes a simplification of Eq. (28), which results in Eq. (29).

$$u(t) = kp_{angle} \cdot Ae(t) \cdot \left(kp \cdot \left(Ve(t) + td \cdot \frac{dVe(t)}{dt} + \frac{1}{ti} \cdot \int_0^t (Ve(t) \cdot dt) \right) \right) \tag{28}$$

$$u(t) = kp_{angle} \cdot Ae(t) \cdot \left(kp \cdot \left(Ve(t) + \frac{1}{ti} \cdot \int_0^t (Ve(t) \cdot dt) \right) \right) \tag{29}$$

where kp_{angle}, kp, td and ti are the constant PID values listed in Table 4, as well as $Ae(t)$ is the angular error or inclination error as a function of time and $Ve(t)$ is the angular velocity error as a function of time. The transfer function of the PID controller in the Laplace domain is expressed in Eq. (30):

$$PID_{Controller} = kp_{angle} \cdot \left(\frac{kp \cdot ti \cdot td \cdot s^2 + kp \cdot ti \cdot s + kp}{ti \cdot s} \right) \tag{30}$$

Table 4
PID constant.

Parameter	Value
Proportional constant for angle (kp_angle)	2.55
Proportional constant for velocity (kp)	15.80
Integrative constant for velocity (ti)	0.35
Derivative constant for velocity (td)	0.00

5.2. Fuzzy logic controller

Fuzzy systems are very suitable for solving problems in which do not exist a simple mathematical model to explain the UAV dynamics or in which nonlinear problems are involved (e.g., due to uneven weight distribution of electronics or UAV dynamics represented by trigonometric functions). To this end, two Fuzzy systems were developed with the Matlab® Fuzzy Toolbox™ aimed at stabilizing: *a*) height in the Z axis, and *b*) roll and pitch in the X and Y axes of the UAV. A FLC based on the Mamdani's linguistic model has been used to implement the height, while two FLCs based on the Mamdani and Takagi-Sugeno-Kang models have been utilized to stabilize the roll and pitch. Furthermore, different strategies have been applied to tune the labels of the FLCs. These include both manual tuning and automatic tuning using genetic algorithms.

5.2.1. FLC for height

This Fuzzy controller is based on the Mamdani model. This type of logic was selected because it is more intuitive (i.e., numerical data is linked to human expressions), uses the same database for all rules, and is more commonly utilized in artificial intelligence control systems. The process followed to generate the Fuzzy models with the Mamdani's linguistic is as follows: fuzzification of the input parameters, evaluation of the linguistic rules, aggregation of the output variables for each rule and defuzzification using the centroid method. The fuzzification process and evaluation of the linguistic rule is based on the use of the T-norm of the minimum as conjunction and implication operators (Eq. (31)):

$$\mu AND(x, y) = \min(\mu A(x), \mu B(y)) \tag{31}$$

where μAnd represents the minimum value of implication and conjunction (i.e., compliance with a rule) based on the lowest value obtained by antecedent A or B. Correspondingly, the FITA method (i.e., First Inter, Then Aggregate) and the centroid method (Eq. (32)) has been used for the defuzzification process. In this way, the gravity center of the rules inferenced of the Fuzzy set is provided as output of the Fuzzy controller.

$$centroid = \frac{\sum_i \mu(x_i) \cdot x_i}{\sum_i \mu(x_i)} \tag{32}$$

where $\mu(x_i)$ is the membership value of the point x_i in the universe of the rule consequent.

The function of the height controller was to maintain the UAV height at a certain level, specifically at 2.5 m, using the ultrasonic sensors as inputs and the BLDC motor as output. The active range of the ultrasonic sensors was between 1.7 and 400 cm, so the input was established as the difference between the height measured and the reference height as described in Eq. (33):

$$\text{error}_{z} = 2.5 - Z \tag{33}$$

The BLDC motor was controlled by an 8-bit PWM output signal with discrete values between 0 and 255. To get this, it was necessary to consider that the zero level —or stable level for the UAV— was not the medium value of the PWM signal. On the contrary, we set the power required to maintain hovering the UAV at 65% at least as in Eq. (34):

$$PWM_{motor} \geq PWM_{max} \text{x} \frac{W_m + W_s + W_e}{T_m} \text{x} 100 \tag{34}$$

The membership functions for the FLC of the UAV height consisted of triangular labels where the universe of discourse for $\text{error}_{z\text{NumberSensor}}$

was [−4.0, 4.0] and for the PWM signal was [0, 255]. The Fuzzy height controller performs a high-level sensory fusion with the height errors obtained by each ultrasound sensor to determine which PWM value assigns to the BLDC motor. The set of rules used is described below and the cutoff points of the membership functions are listed in Table 5.

If error_{z1} *is below and* error_{z2} *is below, then* PWM_{motor} *is high*
If error_{z1} *is below and* error_{z2} *is stable, then* PWM_{motor} *is hover*
If error_{z1} *is below and* error_{z2} *is above, then* PWM_{motor} *is low*
If error_{z1} *is below and* error_{z2} *is below, then* PWM_{motor} *is hover*
If error_{z1} *is below and* error_{z2} *is stable, then* PWM_{motor} *is hover*
If error_{z1} *is below and* error_{z2} *is above, then* PWM_{motor} *is hover*
If error_{z1} *is below and* error_{z2} *is below, then* PWM_{motor} *is high*
If error_{z1} *is below and* error_{z2} *is stable, then* PWM_{motor} *is hover*
If error_{z1} *is below and* error_{z2} *is above, then* PWM_{motor} *is low*

The force required to lift the UAV must be at least 2.0614 N, which is defined by the following equations:

$$\sum F_z = ma_z = 0 \tag{35}$$

$$8F_{sur} + 4F_{flap\_z} + mg = ma_z = 0 \tag{36}$$

$$8|F_{sur}| + 4|F_{sur}|(1 - \cos 45^\circ) - mg = ma_z = 0 \tag{37}$$

In addition, the moment of inertia and efficiency coefficient (K_{eff}) have been determined by CAD simulations. Likewise, the distances and weights of the UAV were determined manually, all of which are shown in Table 6.

5.2.2. FLC for roll and pitch

The stability controller maintains the UAV within a given inclination, either on the X-axis or Y-axis (i.e., roll and pitch). Therefore, it is necessary to use such a controller for each axis. Both controllers have the same set of rules and label configuration. The inputs for each axis are the inclination error (i.e., difference between desired and actual inclination of the UAV) and angular velocity, which are provided by the IMU included in the UAV. The inclination error is measured in degrees (°) and the angular velocity in degrees per second (°/s). The outputs generated by the FLC are the opening degrees of the UAV flaps to get stability. These values are given in a range of ±45° and represent the physical limitations of the minimum and maximum opening of the flaps. The equilibrium point representing the vertical stability of the UAV is 0°, which occurs when the flaps are at 45° with respect to the body of the UAV. The outputs in degrees are transformed into a PWM signal to set the position of the servos that manage the flap opening. This signal has an actuation range from 0 to 255, where 0 represents an opening of 0° and 255 an opening of 90°. Both input and output membership functions are triangular.

5.2.2.1. Manual tunning of the Mamdani model. The first FLC developed is based on the Mamdani's linguistic model, which has been manually tuned. The model options are similar to those of the FLC used for height stability. As in the previous case, the membership functions for both antecedents and consequents (i.e., inputs and outputs, respectively) are triangular, as well as the same methods and operators previously indicated. The membership values are defined in Table 7, which set of rules is as follows:

If DifAng is Stable AND Speed is Negative, then FlapAngle is Clockwise_movement
If DifAng is Stable AND Speed is Zero, then FlapAngle is Zero
If DifAng is Stable AND Speed is Positive, then FlapAngle is CounterClockwise_movement
If DifAng is Negative, then FlapAngle is CounterClockwise_movement
If DifAng is Positive, then FlapAngle is Clockwise_movement
If DifAng is Negative AND Speed is Negative, then FlapAngle is Clockwise_movement
If DifAng is Positive AND Speed is Positive, then FlapAngle is CounterClockwise_movement

Table 5
Fuzzy labels for the height controller.

Labels /Points	P1	P2	P3
$\text{error}_{\text{zNumberSensor}}$			
Below	−400	−400	50
Stable	−50	0	50
Above	−50	400	400
PWM_{Motor}			
High	0	0	165
Hover	110	165	210
Low	165	255	255

Table 6
Parameters of flight.

Parameters	Value	Unit
F_{sur}	2.0614	N
Mass	1.460	Kg
UAV diameter	0.5	m
Vertical distance from gravity center to flap	0.02	m
K_{eff}	0.9	–
Inertia of moment (from 3-D modeling)	0.0095	Kg/m^2
Antitorque	0	N * m
Torque	0	N * m

Table 7
Fuzzy labels for the manual controller.

Labels /Points	P1	P2	P3
Angular difference			
Negative	−45	−45	0
Stable	−15	0	15
Positive	0	45	45
Speed			
Negative	−90	−70	0
Zero	−6	0	6
Positive	0	7	0
Flap angle			
CounterClockwise_movement	−53	−29	−0.5
Zero	−1	0	1
Clockwise_movement	0.5	29	53

5.2.2.2. Genetic tunning of the Mamdani model. The second FLC developed —also based on the Mamdani's linguistic model— has been tuned using a genetic algorithm. For this purpose, the Global Optimization ToolBox of Matlab® was used. Specifically, the 'tunefis' tool from this toolbox was utilized, which enables the tuning of Fuzzy models through several optimization techniques. In this study, a mono-objective genetic algorithm was used for optimization. The parameters supplied to this algorithm to perform the optimization were: *i*) population of 3000 individuals; *ii*) maximum of 500 epochs; *iii*) creation function of the initial population based on a normal distribution; *iv*) crossover function from a binary vector where the values equal to "1″ select the data of the first parent and the values equal to "0″ select the characteristics of the second parent; *v*) selection by tournament was chosen as selection function; and *vi*) random mutation function that takes into account whether the previous mutation was successful or not in order to perform the next mutation. For further details, this configuration makes use of the following Matlab options: 'gacreationuniform', 'crossoverscattered', 'selectiontournament', and 'mutationadaptfeasible'. The evaluation function of the algorithm is described in Eq. (41) of Section 6.B.

An optimized genetic linguistic FLC was obtained by applying this metric to the manual FLC model. The significant distinction with respect to the previous model lies in the value of the labels and rules used, while the implication, conjunction operators and defuzzification methods are the same as the previous models. The membership values for the genetic linguistic FLC are defined in Table 8, whilst the set of rules used in the

Table 8
Fuzzy labels for the genetic Mandani controller.

Labels /Points	P1	P2	P3
Angular difference			
Negative	−88.62	−43.82	0.3052
Stable	−1.718	0.00	15.69
Positive	−0.318	44.60	94.40
Speed			
Negative	−162.0	−70.14	3.82e-5
Zero	−5.61	0.381	0.65
Positive	6.18	51.50	149
Flap angle			
CounterClockwise_movement	−53.88	−44.65	−25.99
Zero	−0.70	−0.19	4.47
Clockwise_movement	26.13	31.59	62.23

genetic linguistic FLC is as follows:

If DifAng is Stable AND Speed is Negative, then FlapAngle is Clockwise_movement

If DifAng is Stable AND Speed is Zero, then FlapAngle is Zero

If DifAng is Stable AND Speed is Positive, then FlapAngle is CounterClockwise_movement

If DifAng is Negative, then FlapAngle is CounterClockwise_movement

If DifAng is Positive, then FlapAngle is Clockwise_movement

If DifAng is Negative AND Speed is Negative, then FlapAngle is Clockwise_movement

If DifAng is Positive AND Speed is Positive, then FlapAngle is CounterClockwise_movement

If Speed is Negative, then FlapAngle is Clockwise_movement

If Speed is Positive, then FlapAngle is CounterClockwise_movement

If DifAng is Negative AND Speed is Zero, then FlapAngle is CounterClockwise_movement

If DifAng is Negative AND Speed is Positive, then FlapAngle is CounterClockwise_movement

5.2.2.3. Genetic tunning of the Sugeno model. The third FLC developed is based on the Takagi-Sugeno-Kang (TSK) or Sugeno model, which has also been tuned using a genetic algorithm. This type of model is based on the use of Fuzzy antecedents or inputs, a set of linear functions as outputs or consequents, and a set of rules to relate Fuzzy inputs to outputs. This model is more suitable for complex and/or higher dimensional systems than the Mamdani-based models. The main difference is that the Sugeno model does not perform complex defuzzification processes (e.g., centroid), which is the weighted average of all the rule outputs. Thus, it is more computationally efficient. The fuzzification process and evaluation of the linguistic rule is based on the use of the T-norm of the product (Eq. (38)) as a conjunction operator and the T-norm of the minimum (Eq. (31)) as an implication operator.

$$\mu Prod(x, y) = x \cdot y \tag{38}$$

where $\mu Prod$ stands for the conjunction of the rule based on the degree of membership of each of the labels (i.e., x and y respectively). As the UAV plant is a complex system characterized by non-linearity, the decision was to employ a Sugeno FLC. To optimize this controller, the same set of parameters utilized previously in the tunefis tool were employed as optimization parameters. The membership values for the Sugeno FLC are defined in Table 9, being the set of rules as follows:

If DifAng is Stable, then FlapAngle is function3

If DifAng is Positive AND Speed is Zero, then FlapAngle is function2

If DifAng is Positive, then FlapAngle is function1

If DifAng is Stable AND Speed is Positive, then FlapAngle is function1

If DifAng is Negative AND Speed is Negative, then FlapAngle is function2

If DifAng is Positive AND Speed is Negative, then FlapAngle is function2

If DifAng is Stable AND Speed is Zero, then FlapAngle is function1

If DifAng is Positive AND Speed is Positive, then FlapAngle is function1

If DifAng is Negative AND Speed is Zero, then FlapAngle is function2

Table 9
Fuzzy labels for the genetic Sugeno controller.

Labels /Points	P1	P2	P3
Angular difference			
Negative	−82.49	−33.30	−1.831
Stable	−37.5	0.00	37.5
Positive	−13.8	−1.112	23.15
Speed			
Negative	−59.01	−27.22	52.09
Zero	−75.00	0.00	75.00
Positive	14.02	22.08	71.67
Flap angle			
function1	42.96	−5.541	29.62
function2	39.28	−1.778	−19.29
function3	16.51	−32.33	−32.71

If DifAng is Stable AND Speed is Zero, then FlapAngle is function2

If Speed is Zero, then FlapAngle is function1 where function1, function2 or function3 has the following structure:

$$FlapAngle = \mathrm{P1} * x + \mathrm{P2} * y + \mathrm{P3} \tag{39}$$

where P1, P2 and P3 are defined for each of the functions in Table 9.

5.2.2.4. Implementation of fuzzy controllers. These FLCs have been validated through the schematic presented in Fig. 6b. Top of figure includes the manually tunned FLC (i.e., therefore referred to as manual FLC), which is highlighted in purple background. It consists of a summation that calculates the inclination error of the UAV. The error is used as input to the manual FLC along with the angular velocity obtained by integrating the angular acceleration determined by the flight model. The output of the manual FLC is equally the position of the UAV flaps. The plant responds to this input by producing an angular acceleration, which must be integrated twice to obtain the UAV's angular position relative to the center of the coordinate axes. The integration of the angular acceleration to obtain the angular velocity and angular position was carried out in the Laplace domain with Simulink®. Meanwhile, the angular velocity and angular position were provided by the IMU for the real UAV. In this way, it is possible to obtain the current inclination of the UAV. The next part of the schematic in Fig. 6b (green background) represents a control loop for a optimized linguistic Fuzzy controller (i.e., genetic Mandani FLC). Finally, the last schematic section in Fig. 6b (orange background) represents a control loop for an optimized Sugeno Fuzzy controller (i.e., genetic Sugeno FLC). This approach is the same as the previous ones, although it includes a saturation block in order to comply with the physical limitations of the UAV's flap openings, which is limited to $\pm 45^{\circ}$.

6. Experimentation

The measurement of the thrust achieved by the combination of the BLDC motor, the propeller and the ducted fan was carried out by a test that consisted in using a digital weighing scale, turning the blade, placing an ammeter to measure the instant current, and gradually increasing the power of the motor through the PWM signal. As shown in Fig. 7a, we obtained a maximum of 1500 g of thrust with 20A of current. This test served to assess the consistency of the design according with the sizing of the UAV from Eq. (26). Fig. 7b shows a test at different flight heights for 550 s. We simultaneously used the two ultrasonic sensors and a simple moving average (SMA) to remove the signal noise considering a window of 20 readings. To this extent, the red line shows the RAW data whilst the blue line shows the filtered data. Fig. 7c shows an example of the IMU. Since the roll and pitch angles typically suffer from the motor vibrations transmitted through the UAV structure because of the high speed, we applied a complementary filter as described in Eq. (40). Experimentally, we found $k = 0.03$ as the optimal value:

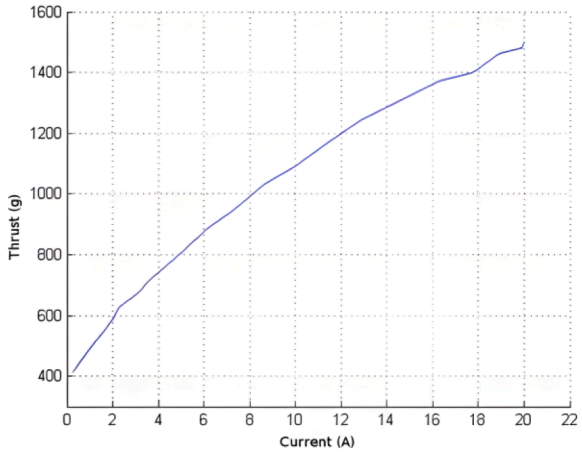

(a)

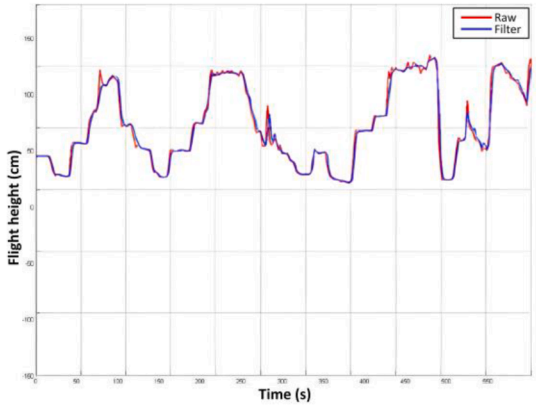

(b)

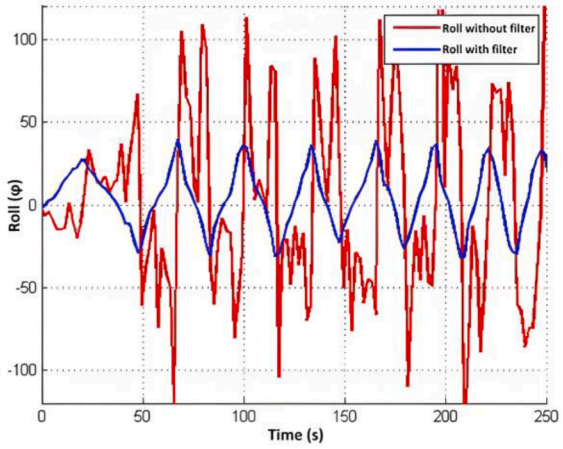

(c)

Fig. 7. Validation of the UAV sensors: (a) thrust vs source current, (b) flight height vs time, and (c) roll angle vs time. .

$$angle = k(angle + gyrData \cdot \Delta t) + (|k-1|) \cdot accData \quad (40)$$

Similarly, we can observe the improvement on the sensor signals where the red line shows the RAW data, and the blue line shows the filtered data (Fig. 7c).

6.1. Validation of system dynamics

A flight simulator was created using Matlab® to validate the system forces present in the UAV. This simulator considers the equations described in Section 3 and uses the inputs of the system forces determined by these equations. The inputs used in the simulation are alpha 1 (a1), alpha 2 (a2), force and simulation time, where alpha 1 represents the opening degrees for the Y-axes of the flaps (i.e., pitch), and alpha 2 means the opening degrees for the X-axes of the flaps (i.e., roll). In both axes, the equilibrium point is 45°, with degrees less than 45° representing clockwise movements and greater than 45° counter-clockwise movements. The force represents the surface force (F_{sur}) applied to the UAV, being necessary 2.0614 N at least to sustain the UAV. Fig. 8 shows the simulation environment created to validate the system dynamics and study flight sequences. As an example, an UAV spiral lift trajectory is shown as a function of the calculated F_{sur} force.

6.2. Validation of system controllers

The stabilization of the UAV with the various PID and FLC controllers was tested with different inclination degrees. The initial angles used were −15°, 15°, −30°, 30°, −45° and 45°. The validation has followed the Simulink schematics presented in Fig. 6. As seen in Fig. 9, the saturated PID controller and the FLC controllers always achieve UAV stability, while the plant without a controller is unstable as expected and never reaches the target angle (i.e., reference at 0°). Moreover, the unsaturated PID also fails to reach the reference desired. They are not included in Tables 10-13 for this reason.

Regarding the stabilization time (Table 10), the fastest controller is the genetic Sugeno FLC. This controller has an average settling time of 1.183 ± 0.267 s. In percentage terms, the improvement provided by the genetic Sugeno FLC is 35.23% faster on average than the saturated PID controller, 51.98% than the genetic Mamdani FLC and 121.58% than the manual FLC.

Regarding the overshoot (Table 11), the results provided by the genetic Sugeno FLC are better than the other controllers. The average overshoot obtained by the genetic Sugeno FLC is 0.10°, corresponding to 0.32% of the target angles. In contrast, the saturated PID, genetic Mamdani FLC and manual FLC achieved overshoot values of 0.39%, 1.18% and 1.42%, respectively. These results confirm that the genetic Sugeno FLC is a more robust controller since it produces a smaller overshoot in a shorter settling time.

Regarding the area under the curve (Table 12), the results indicate that the saturated PID controller is the one that needs less area to achieve the target when reaching the settling time. This controller provides an average area of 2.72°·s, which is the smallest area obtained compared to the other controllers. The genetic Sugeno FLC needs an increment of 0.21% of the area, the genetic Mamdani FLC an increment of 34.02%, and the manual FLC an increment of 2.17%. These findings indicate that, while the genetic Sugeno FLC requires slightly higher area than the saturated PID controller to reach the desired goal, the difference is minimal and it still presents a good performance.

Finally, a compound metric has been calculated to evaluate the performance of each of the stability controllers:

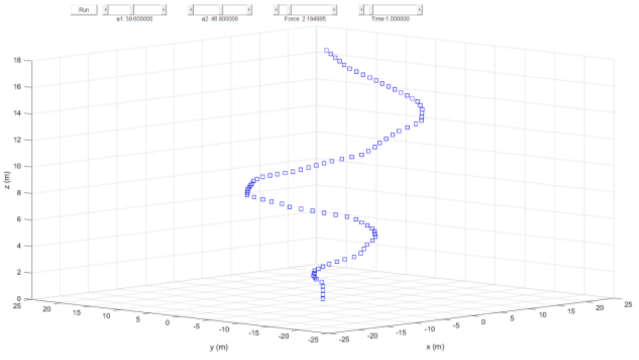

Fig. 8. Flight simulation in Matlab® to validate the dynamics of the UAV system.

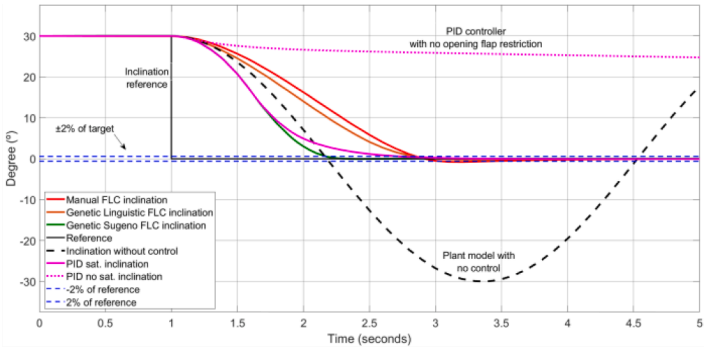

Fig. 9. Evaluation of the FLCs to reach a target angle of o° from an initial angle of 30°.

Table 10
Stabilization time of controllers.

Angle (°)	Saturated PID (s)	Manual FLC (s)	Genetic Mandani FLC (s)	Genetic Sugeno FLC (s)
−15	1.6	1.9	1.289	0.884
15	1.6	1.9	1.8	0.886
−30	1.8	2.5	1.7	1.191
30	1.8	2.429	1.9	1.173
−45	1.4	3.5	2.0	1.499
45	1.4	3.5	2.1	1.466
Average	1.6	2.622	1.798	1.183
Dev. Std.	0.179	0.726	0.287	0.267
Diff. (s)	0.417	1.438	0.615	0.00
Diff. (%)	35.23	121.58	51.98	0.00

Note: Diff. (s) stand for the settling time difference for each controller against the genetic Sugeno FLC. The same occurs for Diff. (%).

$$metric = 0.9 * St + 0.05 * \left(\frac{AUC}{1000}\right) + 0.05 * |Os| \quad (41)$$

where *St* is the settling time measured in seconds in which the system achieves ±2% of the target signal and remains within this ±2%. At this point, the system can be considered to have reached the stability; *AUC* is the area that encloses the curve generated by the stabilization signal since the system reaches the settling time until the end of the simulation time; and *Os* is the maximum percentage of inclination excess reached by the system. Note that *AUC* has been normalized and divided by 1000 to avoid having a greater weight on the rest of the parameters.

Regarding the compound metric, it is observed that the controller that achieves the best performance is the genetic Sugeno FLC with a value of 6.49 *vs* 8.76 for the saturated PID controller, 10.07 for the genetic Mamdani FLC and 15.19 for the manual FLC. Thus, the genetic Sugeno FLC provides an enhancement of 35.03% in relation to the saturated PID controller, 55.19% to the genetic Mamdani FLC, and 134.21% to the manual FLC. A summary of results is listed in Table 13, which indicates that the model that achieves the best performance is the genetic Sugeno FLC. This suggests that the good performance of the controller in the stabilization of the non-linear plant of the UAV can be attributed to the linearization carried out for each of the rules by the Sugeno model.

Table 12
Area under the curve of controllers.

Angle (°)	Saturated PID (°·s)	Manual FLC (°·s)	Genetic Mandani FLC (°·s)	Genetic Sugeno FLC (°·s)
−15	1.4928	1.7103	2.9228	2.2351
15	1.4928	1.7097	1.2596	1.8013
−30	2.682	3.1543	2.5672	2.6648
30	2.117	4.0715	2.4708	3.1924
−45	4.6937	3.0972	4.4200	2.8862
45	3.8444	2.9341	8.2359	3.5775
Average	2.7204	2.7795	3.6461	2.7261
Dev. Std.	1.3067	0.9189	2.4669	0.6431
Diff. (°·s)	0.00	0.0590	0.9256	0.0058
Diff. (%)	0.00	2.17	34.0	0.21

Note: Diff. (°·s) represents the difference in the area under the curve for each controller against the saturated PID controller. The same occurs for Diff. (%).

Table 13
Compound metric of controllers.

Angle (°)	Saturated PID	Manual FLC	Genetic Mandani FLC	Genetic Sugeno FLC
−15	1.4576	1.7101	1.2427	0.8147
15	1.4576	1.7101	1.6472	0.7946
−30	1.6287	2.3921	1.5638	1.1115
30	1.6287	2.3170	1.7525	1.0620
−45	1.2929	3.5658	1.8747	1.3769
45	1.2926	3.496	1.9845	1.3233
Sum	8.7581	15.1911	10.0654	6.486
Diff.	2.2721	8.7051	3.5794	0.00
Diff. (%)	35.03	134.21	55.19	0.00

Note: Diff. represents the difference in the metric for each controller against the genetic Sugeno FLC. The same occurs for Diff. (%).

Table 11
Overshoot of controllers.

Angle (°)	Saturated PID (°)	Saturated PID (%)	Manual FLC (°)	Manual FLC (%)	Genetic Mandani FLC (°)	Genetic Mandani FLC (%)	Genetic Sugeno FLC (°)	Genetic Sugeno FLC (%)
−15	0.0525	0.35	0.00	0.00	0.2478	1.652	0.0576	0.384
15	−0.0525	0.35	0.00	0.00	−0.0816	0.544	0.00	0.00
−30	0.513	0.171	0.8515	2.838	0.2018	0.6727	0.2386	0.7953
30	−0.0513	0.171	−0.7858	2.619	−0.2545	0.8483	−0.037	0.123
−45	0.2939	0.6531	3.7409	8.3131	0.6706	1.4902	0.2463	0.5473
45	−0.2914	0.64756	−3.1126	6.9169	−0.8468	1.8818	−0.0367	0.08156
Average	0.1322	0.3904	1.4151	3.4479	0.3839	1.1815	0.1027	0.3219
Dev. Std.	0.1243	0.2166	2.2336	3.4796	0.5176	0.5627	0.1319	0.2602

7. Conclusions and future research

Research in robotics is currently heading towards ever more profitable fields of scientific interest as the UAVs. Despite of the variety of approaches, most of them are majorly based on classical fixed-wing aircrafts and multirotor VTOLs. To make a significant contribution in this field, this paper presented the design and mechanical construction of a small-sized UAV based on the Coandă effect, a well-known aerodynamic principle not sufficiently investigated and utilized in UAVs. Its novel approach, based on a single rotor, fixed rudders and four side flaps, was aimed at improving the capabilities of previous Coandă systems (i.e., cost, sensing, communication, and flight control software). Amid the most significant differences, we developed a virtual instrument in LabVIEW™ to wirelessly monitor and control both sensors and actuators through an Arduino NANO microcontroller.

In addition, we designed several Fuzzy logic controllers based on Matlab® to correct the error height, and pitch and roll. The main advantage of using a controller based on Fuzzy logic, unlike others as the PID control, is that it usually works better when the model of the system is complex or non-linear. Therefore, using the proposed method, it can be obtained controllers that describe the behavior of UAVs based on the Coandă effect in a simpler and more intuitive way. To validate the system dynamics, this work presented different tests considering the control of the flight height, pitch and roll according with the sizing of the UAV system (i.e., thrust vs weight, flight height vs time, and roll/pitch vs time). Moreover, a comprehensive experimentation was conducted to validate the performance of various Fuzzy controllers based on Mamdani and Sugeno models —both manually tuned and optimized with genetic algorithms— against a PID controller. The aim was to determine which type of model provides best achievement with respect to the constructed UAV. The results showed that a Fuzzy controller based on the Sugeno model is 0.417 s (35.23%) faster than a PID controller. It was also shown that this controller has a lower overshoot than the PID and —through a proposed metric— it has been shown that the Fuzzy controller is more robust than the PID controller. Both the source codes of the dynamic model for Matlab® and the Fuzzy/PID controllers for Simulink are offered as a contribution to this research at https://github.com/JMLozano/UAV_UHU_simulation.

To improve this research, future works are aimed at including GPS readings to allow periodical calibrations and reduce the accumulative error of the IMU on flight. This could provide an accuracy within the order of centimeters when the Galileo satellite network be fully operational by 2020. In this sense, the use of a Kalman filter would improve the attitude control from the accelerometer and the gyroscope inputs. Also, a camera on board could enhance the flight control capability by applying machine vision techniques. As for the communication, this would require an IEEE 802.11-based link to provide a wider bandwidth. It will also let to enhance the native coverage and increase the control range compared with Bluetooth®. Finally, other efforts will be focused on increasing the battery life. Although the additional payload would increase the total weight, we will consider constructing the UAV with carbon fiber, a more resistant and lighter material but more expensive than the Balsa wood. In terms of UAV control, the investigation will focus on determining whether the implementation of a Fuzzy-PID controller can enhance these results. Additionally, the applicability of Linear Matrix Inequality (LMI) controllers will be explored.

CRediT authorship contribution statement

Tomás de J. Mateo Sanguino: Conceptualization, Funding acquisition, Investigation, Methodology, Project administration, Resources, Supervision, Writing – original draft, Writing – review & editing. **José M. Lozano Domínguez:** Data curation, Formal analysis, Methodology, Software, Validation, Writing – original draft, Writing – review & editing.

Declaration of competing interest

The authors declare the following financial interests/personal relationships which may be considered as potential competing interests: This work has been financed by the University of Huelva within the scope of the Research and Transfer Policy Strategy and the research group TEP-192 on Control and Robotics.

Data availability

Data will be made available on request.

Acknowledgments

We would like to express our very great appreciation to M.A. Pérez Bocanegra, D. Carrasco Pérez, C. Jiménez Gómez, P. Rodríguez Díaz and Z. Mahmoud Sánchez for their valuable and constructive work that helped to improve this research.

References

[1] T.J. Mateo Sanguino, 50 Years of Rovers for Planetary Exploration: a Retrospective Review for Future Directions, Rob. Auton. Syst. 94 (2017) 172–185.
[2] B.B.V.L. Deepak, P. Singh, A survey on design and development of an unmanned aerial vehicle (quadcopter), Intern. J. Intelligent Unmanned Systems 4 (2) (2016) 70–106.
[3] N.V. Hoffer, C. Coopmans, A.M. Jensen, Y.Q. Chen, A Survey and Categorization of Small Low-Cost Unmanned Aerial Vehicle System Identification, J. Intell. Robot. Syst. 74 (1) (2014) 129–145.
[4] S. Gupte, P.I. Mohandas, J.M. Conrad, A survey of quadrotor Unmanned Aerial Vehicles, in: Proc. IEEE Southeastcon, Orlando, FL, 2012, pp. 1–6.
[5] F. Kendoul, Survey of advances in guidance, navigation, and control of unmanned rotorcraft systems, J. Field Robotics 29 (2) (2012) 315–378.
[6] L. Dinca, J.I. Corcau, C.M. Larco, C. Rotaru, I.R. Adochiei, About Aerodynamic Design of a Coanda Effect UAV, in: E-Health and Bioengineering Conference (EHB), Iasi, Romania, 2019, pp. 1–4.
[7] H. Coanda, "Propelling device," in US Patent no. 2,108,652 A. USA, 1938.
[8] B. Lindenbaum, W. Blake, "The VZ-9 Avrocar", Tech. Rep., no date.
[9] F. Nedelcuţ, Coandă Effect aerodyne – A new platform concept for a fluvial and ecological remote sensing aerial vehicle, Tech. Rep., University of Galaţi, Romania (2014).
[10] R. Collins, Coanda - A new Airspace Platform for UAVs, in: 17th Intern. Conf. Unmanned Air Vehicle Systems, Bristol, UK, 2002.
[11] G., Hatton, and S. McIntosh, "Craft having flow-producing rotor and gyroscopic stability," in UK Patent no. 2,424,405. GB, 2005.
[12] J.L. Naudin, The Coanda Effect Saucer UAV, Tech. Rep. (2010).
[13] C. Barlow, D. Lewis, S.D. Prior, Odedra S, M.A. Erbil, M. ñ.m Karamanoglu, R. Collins, Investigating the use of the coanda effect to create novel unmanned aerial vehicles, in: Proc. Intern. Conf. Manufacturing and Engineering Systems, 2009, pp. 386–391.
[14] D. Kemp, AA 2006: FanTail 5000 prototype flight, Tech. Rep. (2006).
[15] F. Nedelcuţ, S.G. Constantinescu, LUAV's are the right approach for surveillance civil missions, in: Intern. Conf. Scientific Papers Brasov, Romania, 2011, pp. 1237–1240.
[16] A. White, Upgrades for gMAV in light of Iraq ops, Tech. Rep. (2010).
[17] Ltd. Aesir, Coanda-effect VTOL UAV, Tech Rep. (2009) [Online], http://diydrones.com/video/aesir-coanda-effect-vtol-uav.
[18] O. Crivoi, I. Doroftei, F. Adascalitei, A Survey on Unmanned Aerial Vehicles Based on Coanda Effect, TEHNOMUS (2013) 338–344.
[19] H. Djojodihardjo, M.F.A. Hamid, S. Basri, F.I. Romili, D.L.A. Abdul Majid, Numerical simulation and analysis of Coandă effect circulation control for wind-turbine application considerations, IIUM Engineering J 12 (2011) 51–58.
[20] M. Petrolo, E. Carrera, M. D'Ottavio, C. de Visser, Z. Pátek, Z. Janda, On the development of the Anuloid, a disk-shaped VTOL aircraft for urban areas, Advances in Aircraft and Spacecraft Science 1 (3) (2014) 353–378.
[21] M.E. Haque, M.S. Hossain, M. Assad-Uz-Zaman, M. Mashud, Design and Construction of an Unmanned Aerial Vehicle Based on Coanda Effect, in: Proc. Intern. Conf. Mechanical Engineering and Renewable Energy, Chittagong, Bangladesh, 2015.
[22] A. Banazadeh, M. Behroo, Development, instrumentation, and dynamics identification of a coanda air vehicle, IEEE Aerospace and Electronic Systems Magazine 30 (10) (2015) 4–12.
[23] H. Lee, S. Han, H. Lee, J. Jeon, C. Lee, Y.B. Kim, S.H. Song, H.R. Choi, Design Optimization, Modeling, and Control of Unmanned Aerial Vehicle Lifted By Coandă Effect, IEEE/ASME Trans. Mechatronics 22 (3) (2017) 1327–1336.
[24] Z. Siddiqi, J.W. Lee, Experimental and numerical study of novel Coanda-based unmanned aerial vehicle, J. Eng. Appl. Sci. 69 (76) (2022).

[25] N. Kelly, Z. Siddiqi, J.W. Lee, Computational Fluid Dynamics Analysis and Optimization of the Coanda Unmanned Aerial Vehicle Platform, International Journal of Mechanical and Mechatronics Engineering 14 (12) (2021) 592–597.
[26] I. Cîrciu, C. Rotaru, Theoretical and practical aspects of the Coandă effect applied in aeronautics, in: MATEC Web of Conferences 290, 2019, p. 06003.
[27] Y.H. Pheh, S. Kyi Hla Win, S. Foong, Spherical Indoor Coandă Effect Drone (SpICED): A Spherical Blimp sUAS for Safe Indoor Use, Drones 6 (9) (2022) 260.
[28] D. Shin, H. Kim, J. Gong, U. Jeong, Y. Jo, E. Matson, Stealth UAV through Coandă Effect, in: Fourth IEEE International Conference on Robotic Computing (IRC), Taichung, Taiwan, 2020, pp. 202–209.
[29] A. Briod, P. Kornatowski, J.C. Zufferey, D. Floreano, A collision-resilient flying Robot, J. of Field Robotics 31 (4) (2014) 496–509.
[30] Z. Zhao, B. Zhang, H.O. Lim, Development of a Coanda-drone with High Level of Safety Using Coanda Effect, in: 8th International Symposium on System Security, Safety, and Reliability (ISSSR), Chongqing, China, 2022, pp. 14–19.
[31] B. Uragun, Energy Efficiency for Unmanned Aerial Vehicles, in: 10th Intern. Conf. Machine Learning and Applications and Workshops 2, 2011, pp. 316–320.
[32] H. Chao, Y. Luo, L. Di, Y. Chen, Fractional Order Flight Control of a Small Fixed-Wing UAV: Controller Design and Simulation Study, in: Proc. ASME 2009 Intern. Design Engineering Technical Conf. & Computers and Information in Engineering Conf., 2009, pp. 621–628.
[33] D. Kingston, R. Beard, T. McLain, M. Larsen, W. Ren, Autonomous Vehicle Technologies for Small Fixed-Wing UAVs, J. Aerospace Computing Information and Communication 2 (1) (2005) 92–108.
[34] J.F. Gomez, M. Jamshidi, Fuzzy Adaptive Control for a UAV, J. Intell. Robot. Syst. 62 (2011) 271–293.
[35] D. Stojcsics, Fuzzy Controller for Small Size Unmanned Aerial Vehicles, in: 10th IEEE Jubilee Intern. Symp. Applied Machine Intelligence and Informatics, 2012, pp. 26–28.
[36] K.S. Kumar, M. Rasheed, R.M.M. Kumar, Design and Implementation of Fuzzy Logic Controller for Quad Rotor UAV, in: 2nd Intern. Conf. Research in Science, Engineering and Technology, 2014, pp. 114–120.
[37] J.C. Ervin, S.E. Alptekin, D.J. DeTurris, Optimization of the Fuzzy Logic Controller for an Autonomous UAV, in: Proc. Joint 4thEuropean Society of Fuzzy Logic and Technology Conf, Barcelona, Spain, 2005.
[38] H. Coanda, "Device for Deflecting a Stream of Elastic Fluid Projected into an Elastic Fluid," in US Patent no. 2,052,869. USA, 1936.
[39] H. Coanda, "Lifting Device Coanda Effect," in US Patent no. 3,261,162. USA, 1936.
[40] R. Collins, Coanda Flight Controls, in: 18th Intern. Conf. Unmanned Air Vehicle Systems, Bristol, UK, 2003.
[41] J.M. Andújar Márquez, T.J. Mateo Sanguino, F.J. Aguilar Nieto, J.J. Chica Barrera, M.F. Mola Mateos, An Image Acquiring, Processing and Transfer System over Bluetooth for an Educational Robotic Platform, in: Robótica 2007 - 7th Conf. Mobile Robots and Competitions, Albufeira (Portugal), 2007, pp. 1–6.

Tomás de J. Mateo Sanguino is an Electronic Engineer and Master in University Teaching. From 1998 to 2004, he had a scholarship at the National Institute of Aerospace Technology (INTA) and worked as a hired engineer at the Spanish National Research Council (CSIC). Since 2004 he works in the Dep. Electronic Engineering, Computer Systems and Automatics at the University of Huelva, currently being as a full-time Associate Professor. He has taken part as a researcher in 21 R&D projects and has authored and co-authored over 60 publications in different journals and congresses indexed in Scopus, among which he counts on 40 papers in the SCI. He received the Ph.D. degree in Electronic Engineering in 2010. His current research interests include robotics and mechatronics.

José Manuel Lozano Domínguez received the Computer Engineering degree in 2016 and Master in Computer Engineering in 2018 from the University of Huelva. He has been an Engineer hired by the Spanish Ministry of Education, Culture and Sport in 2015 and temporary teacher of the Master in Remotely Piloted Aircraft Systems in 2017. Since 2018 he is teacher in the Dep. Electronic Engineering, Computer Systems and Automatics at the University of Huelva. His research interests include electronics and intelligent control systems. He received the Ph.D. degree in Industrial and Environment Science and Technology in 2022.